LA-UR- 09-06779

Approved for public release; distribution is unlimited.

Title:	Mesoscopic Modeling of Multi-Physicochemical Transport Phenomena in Porous Media
Author(s):	Qinjun Kang Moran Wang Partha P. Mukherjee Peter C. Lichtner
Intended for:	Advances in Mechanical Engineering Special Issue: Micro/Nanotransport Phenomena in Renewable Energy and Energy Efficiency

Form 836 (7/06)

Mesoscopic Modeling of Multi-Physicochemical Transport Phenomena in Porous Media

Qinjun Kang, Moran Wang, Partha P. Mukherjee, and Peter C. Lichtner

Computational Earth Science Group

Los Alamos National Laboratory, Los Alamos, NM 87545

Abstract

We present our recent progress on mesoscopic modeling of multi-physicochemical transport phenomena in porous media based on the lattice Boltzmann method. Simulation examples include injection of CO_2 saturated brine into a limestone rock, two-phase behavior and flooding phenomena in polymer electrolyte fuel cells, and electroosmosis in homogeneously charged porous media. It is shown that the lattice Boltzmann method can account for multiple, coupled physicochemical processes in these systems and can shed some light on the underlying physics occurring at the fundamental scale. Therefore, it can be a potential powerful numerical tool to analyze multi-physicochemical processes in various energy, earth, and environmental systems.

1. Introduction

Multi-physicochemical transport phenomena in porous media are ubiquitous, particularly in various energy, earth, and environment systems. One example is the disposal of supercritical CO_2 in geologic formations, the most promising near-term solution to the problem of reducing carbon emissions into the atmosphere [1]. Experimental analyses of the long-term fate of CO_2 after injection into the geologic formations are not possible with relatively short-term laboratory experiments. Therefore it is necessary to employ comprehensive numerical models that incorporate multiple physicochemical processes involving interactions between the injected CO_2, the brine in the pore spaces, and the minerals lining the pores. Supercritical CO_2, as a buoyant and slightly miscible fluid, once injected, displaces brine from the pore space in a complex pattern. At the interface with brine, CO_2 dissolves into the brine to form carbonic acid that can react with and dissolve minerals eventually leading to mineral precipitation further along the flow path. Clearly, there are multiple physics processes involved, including hydrodynamics, thermodynamics, chemical dynamics, and electrodynamics (because the surface of most natural media is charged). All these processes are ultimately governed by pore-scale interfacial phenomena, which occur at scales of microns. However, because of the wide disparity in scales ranging from pore to field, a continuum formulation based on spatial averages taken over length scales much larger than typical pore and mineral grain sizes is often utilized, implying the existence of a representative elemental volume (REV) [2]. As a result, spatial heterogeneities at smaller scales are unresolved and the aggregate effects of the porescale (mesoscopic scale) processes are taken into account through various effective constitutive parameters. One of the goals of performing pore-scale simulations is to obtain values for these constitutive parameters through upscaling the pore-scale results. Other goals are to identify key parameters and

physicochemical processes that control macroscopic phenomena, and to validate continuum descriptions.

Another example is fuel cells, and in particular polymer electrolyte fuel cells (PEFCs). In PEFCs, the catalyst layer (CL) is the host to several competing transport mechanisms involving charge (proton and electron), species (oxygen, nitrogen, water vapor), and liquid water transport. The multi-faceted functionality of a gas diffusion layer (GDL) includes reactant distribution, liquid water transport, electron transport, heat conduction and mechanical support to the membrane-electrode-assembly. Despite tremendous recent progress in enhancing the overall cell performance, a pivotal performance limitation in PEFCs is manifested in terms of mass transport loss originating from suboptimal liquid water transport and resulting flooding in the constituent components [3]. In recent years, several macroscopic computational models for multiple-physicochemical transport processes in PEFCs [4-10] have been developed. These macroscopic models, again are based on the theory of volume averaging and treat the catalyst layer and gas diffusion layer as macro-homogeneous porous layers. Due to their macroscopic nature, the current models fail to resolve the influence of the structural morphology of the CL and GDL on the underlying physics. Mesoscopic modeling is critical to understanding the overall structure-wettability-transport interactions as well as the underlying multi-physicochemical processes in the CL and GDL, and hence is a useful tool for design and optimization of microstructures of electrodes for better performance and durability.

In this paper, we review our recent work on mesoscopic modeling of multi-physicochemical processes in porous media, based on the lattice Boltzmann method (LBM), a relatively new numerical method for simulating fluid flows and modeling physics in fluids [11]. Originating from the classical statistical physics, LBM is a mesoscopic method based on

63 simplified kinetic equations. In the LBM, the fluid is modeled as a collection of fictitious-
64 particles propagating and colliding over a discrete lattice domain. Mesoscopic continuity and
65 momentum equations can be obtained from this propagation-collision dynamics through a rigors
66 mathematical analysis. The particulate nature and local dynamics provide advantages for
67 complex boundaries and parallel computation. In addition, the kinetic nature of the LBM makes
68 it easy to account for new physics in the LBM framework, which is especially useful for
69 modeling multi-physicochemical phenomena. In Section 2, the partial differential equations
70 governing fluid flow, transport of reactive species and electric potential, as well as mineral
71 reactions in porous media will be given. In Section 3, the implementation of the LBM to solve
72 these governing equations will be presented. Some simulation examples will be given in Section
73 4 and concluding remarks in Section 5.

74 **2. Governing Equations**

75 ***2.1 Continuity and momentum equations***

76 For isothermal incompressible fluid flow, the continuity and momentum equations can be
77 written as [12]

78 $$\nabla \cdot \mathbf{u} = 0, \tag{1}$$

79 $$\rho \frac{\partial \mathbf{u}}{\partial t} + \rho \mathbf{u} \cdot \nabla \mathbf{u} = -\nabla p + \rho \nu \nabla^2 \mathbf{u} + \mathbf{F}, \tag{2}$$

80 where ρ represents the density of the fluid, t the time, $\mathbf{u}$ the velocity vector, p the pressure, ν
81 the kinetic viscosity, and $\mathbf{F}$ the body force density which may include all the effective body
82 forces.

2.2 Transport equations for aqueous species and electrical potential

For the *i*th ion species in the solute, the mass conservation equation describing transport and reaction can be written in the general form [13]:

$$\frac{\partial C_i}{\partial t} + \nabla \cdot \mathbf{J}_i + \lambda_i C_i = R_i, \tag{3}$$

where C_i denotes the ionic concentration, $\mathbf{J}_i$ the species flux, λ_i a radioactive decay constant, and R_i the rate at which the *i*th species is produced or consumed by chemical reactions. The flux $\mathbf{J}_i$, consisting of contributions from advection, diffusion, and electrochemical migration terms, has the form [13]

$$\mathbf{J}_i = -\frac{ez_i D_i}{kT} C_i \nabla \Psi - D_i(\nabla C_i + C_i \nabla \ln \gamma_i) + C_i \mathbf{u}, \tag{4}$$

where the first term on the right refers to electrochemical migration, the second term to aqueous diffusion, and the last term to advective transport. Here z_i, D_i and γ_i denote the ion algebraic valence, the diffusivity and the activity coefficient of the *i*th species, respectively; and e, k, and T denote the absolute charge of electron, the Boltzmann constant and the absolute temperature, respectively. The quantity Ψ represents the local electrical potential caused by the ionic distribution which is governed by the Poisson equation

$$\nabla \cdot (\varepsilon_r \varepsilon_0 \nabla \Psi) = -\rho_e = -\sum_i ez_i C_i, \tag{5}$$

where ε_r is the local dimensionless fluid dielectric constant, ε_0 the permittivity of a vacuum, and ρ_e the net charge density. Assuming no radiation and constant activity coefficient and substituting Eq. (5) into (3), we have

103 $$\frac{\partial C_i}{\partial t} + \mathbf{u} \cdot \nabla C_i = D_i \nabla^2 C_i + \frac{e z_i D_i}{kT} \nabla \cdot \left(C_i \nabla \Psi \right). \quad (6)$$

104 This is the Nernst-Planck equation [14], where $\mathbf{F}$ can be any kind of effective body force. In this
105 contribution we only consider the static electrical force from an external electric field. The
106 general form of electrical force in electrokinetic fluids can be expressed as:

107 $$\mathbf{F}_E = -\rho_e \nabla \Psi_{ext}, \quad (7)$$

108 where Ψ_{ext} is the external electrical potential field.

109 When the ionic convection is negligible and the electric potential is continuously
110 derivable, Eq. (6) has a simple steady-state solution for dilute electrolyte solutions:

111 $$C_i = C_{i,\infty} e^{-\frac{e z_i \Psi}{kT}}. \quad (8)$$

112 Substituting Eq. (8) into Eq. (5) yields the nonlinear PB equation [15]

113 $$\nabla^2 \Psi = -\frac{1}{\varepsilon_r \varepsilon_0} \sum_i e z_i C_{i,\infty} \exp\left(-\frac{e z_i}{kT} \Psi \right). \quad (9)$$

114 ***2.3 Equations for mineral reaction rates***

115 Heterogeneous reactions between aqueous species and minerals at the pore-mineral
116 interface are given by [16]

117 $$AD \left. \frac{\partial \Psi_j}{\partial n} \right|_s = \sum_s \nu_{js} A_s \hat{I}_s(s), \quad (10)$$

118 where n denotes the unit normal perpendicular to the fluid-mineral interface pointing toward the
119 fluid phase, D denotes the aqueous diffusion coefficient assumed to be the same for all species
120 for simplicity, and $\hat{I}_s(s)$ denotes the reaction flux of the sth mineral at its surface, taken as
121 positive for precipitation and negative for dissolution. The total surface area A across which
122 diffusion takes place equal to the sum of individual mineral surface areas A_s

$$A = \sum_s A_s \tag{11}$$

3. Lattice Boltzmann Model Implementation

3.1 Incompressible lattice Boltzmann model for single phase flow

In order to eliminate compressible effects in the conventional LBM, here we use an incompressible LB model constructed by Guo et al. [17]. The pore-scale flow of a single aqueous fluid phase is simulated by the following evolution equation:

$$f_\alpha(\mathbf{x} + \mathbf{e}_\alpha \delta_t, t + \delta_t) = f_\alpha(\mathbf{x}, t) - \frac{f_\alpha(\mathbf{x}, t) - f_\alpha^{eq}(\mathbf{x}, t)}{\tau}. \tag{12}$$

In the above equation, δ_t is the time increment, f_α the distribution function along the α direction in velocity space, f_α^{eq} the corresponding equilibrium distribution function, and τ the dimensionless relaxation time. For the commonly used two-dimensional, nine-speed LB model (D2Q9), the discrete velocities $\mathbf{e}_\alpha$ have the following form:

$$\mathbf{e}_\alpha = \begin{cases} (0,0) & \alpha = 0, \\ (\cos\theta_\alpha, \sin\theta_\alpha)c, \quad \theta_\alpha = (\alpha - 1)\pi/2 & \alpha = 1-4, \\ \sqrt{2}(\cos\theta_\alpha, \sin\theta_\alpha)c, \quad \theta_\alpha = (\alpha - 5)\pi/2 + \pi/4 & \alpha = 5-8. \end{cases} \tag{13}$$

For the incompressible LB model, the equilibrium distribution is defined by Guo et al. [17]:

$$f_\alpha^{eq} = \begin{cases} -4\sigma \dfrac{p}{\rho c^2} + s_\alpha(\mathbf{u}), & \alpha = 0, \\ \lambda \dfrac{p}{\rho c^2} + s_\alpha(\mathbf{u}), & \alpha = 1-4, \\ \gamma \dfrac{p}{\rho c^2} + s_\alpha(\mathbf{u}), & \alpha = 5-8, \end{cases} \tag{14}$$

where σ, λ and γ are the parameters satisfying

139

$$\lambda+\gamma=\sigma$$

140 $$\lambda+2\gamma=\frac{1}{2}, \tag{15}$$

141 and

142 $$s_\alpha(\mathbf{u})=\omega_\alpha\left[3\frac{\mathbf{e}_\alpha\cdot\mathbf{u}}{c^2}+9\frac{(\mathbf{e}_\alpha\cdot\mathbf{u})^2}{2c^4}-\frac{3\mathbf{u}^2}{2c^2}\right]. \tag{16}$$

143 In these equations, $c = \delta x/\delta t$, where δx is the space increment, and p and $\mathbf{u}$ are the

144 pressure and velocity of the fluid, respectively. The corresponding weight coefficients are

145 $$\omega_\alpha=\begin{cases}4/9, & \alpha=0,\\ 1/9, & \alpha=1-4,\\ 1/36, & \alpha=5-8.\end{cases} \tag{17}$$

146 Eq. (12) has been shown to recover Eqs. (1, 2) [17], with the velocity and pressure given

147 by

148 $$\mathbf{u}=\sum_{\alpha=1}^{8}\mathbf{e}_\alpha f_\alpha\,, \tag{18}$$

149 and

150 $$\frac{p}{\rho}=\frac{c^2}{4\sigma}\left[\sum_{\alpha=1}^{8}f_\alpha+s_0(\mathbf{u})\right], \tag{19}$$

151 respectively.

152 ***3.2 Lattice Boltzmann model for two phase flow***

153 The interaction-potential model, originally proposed by Shan and Chen [18], and

154 henceforth referred to as the S-C model, introduces k distribution functions for a fluid mixture

155 comprising of k components. Each distribution function represents a fluid component and

156 satisfies the evolution equation. The non-local interaction between particles at neighboring lattice

157 sites is included in the kinetics through a set of potentials. The LB equation for the kth

158 component can be written as:

159 $$f_i^k(\mathbf{x}+\mathbf{e}_i\delta_t, t+\delta_t) - f_i^k(\mathbf{x},t) = -\frac{f_i^k(\mathbf{x},t) - f_i^{k(eq)}(\mathbf{x},t)}{\tau_k}, \tag{20}$$

160 where $f_i^k(\mathbf{x},t)$ is the number density distribution function for the kth component in the ith

161 velocity direction at position $\mathbf{x}$ and time t, and δ_t is the time increment. In the term on the right-

162 hand side, τ_k is the relaxation time of the kth component in lattice unit, and $f_i^{k(eq)}(\mathbf{x},t)$ is the

163 corresponding equilibrium distribution function.

164 The phase separation between different fluid phases, the wettability of a particular fluid

165 phase to the solid, and the body force, are taken into account by modifying the velocity used to

166 calculate the equilibrium distribution function. An extra component-specific velocity due to

167 interparticle interaction is added on top of a common velocity for each component. Interparticle

168 interaction is realized through the total force, $\mathbf{F}_k$, acting on the kth component, including

169 fluid/fluid interaction, fluid/solid interaction, and external force. More details can be found in

170 [19, 20] .

171 The continuity and momentum equations can be obtained for the fluid mixture as a single

172 fluid using Chapman-Enskog expansion procedure in the nearly incompressible limit:

173 $$\left.\begin{aligned} &\frac{\partial \rho}{\partial t} + \nabla\cdot(\rho\mathbf{u}) = 0 \\ &\rho\left[\frac{\partial \mathbf{u}}{\partial t} + (\mathbf{u}\cdot\nabla)\mathbf{u}\right] = -\nabla p + \nabla\cdot[\rho\nu(\nabla\mathbf{u} + \mathbf{u}\nabla)] + \rho\mathbf{g} \end{aligned}\right\} \tag{21}$$

174 where the total density and velocity of the fluid mixture are given, respectively, by:

175 $$\left.\begin{aligned} &\rho = \sum_k \rho_k \\ &\rho\mathbf{u} = \sum_k \rho_k \mathbf{u}_k + \frac{1}{2}\sum_k \mathbf{F}_k \end{aligned}\right\} \tag{22}$$

with a non-ideal gas equation of state given by [21]:

3.3 Lattice Boltzmann model for transport of reactive solutes

In a previous article, Kang et al. [22] have derived the following LB equation for the total primary species concentrations for chemical systems with reactions written in canonical form:

$$G_{\alpha j}(\mathbf{x}+\mathbf{e}_\alpha \delta_t, t+\delta_t) = G_{\alpha j}(\mathbf{x},t) - \frac{G_{\alpha j}(\mathbf{x},t) - G_{\alpha j}^{eq}(\Psi_j, \mathbf{u})}{\tau_{\alpha\eta}}, (j = 1,..., N_C), \qquad (23)$$

where N_C is the number of primary species, Ψ_j is the total concentration of the j th primary species, $G_{\alpha j}$ is its distribution function along the α direction, $G_{\alpha j}^{eq}$ is the corresponding equilibrium distribution function, $\mathbf{e}_\alpha$ are velocity vectors, δ_t is the time increment, and $\tau_{\alpha\eta}$ is the dimensionless relaxation time.

It has been shown that the above equation can recover the following pore-scale advection-diffusion equation for Ψ_j [23]:

$$\frac{\partial \Psi_j}{\partial t} + (\mathbf{u}\cdot\nabla)\Psi_j = \nabla\cdot\left(D\nabla\Psi_j\right). \qquad (24)$$

This equation is the same as Eq. (6) except that here the electrochemical migration is neglected. Assuming the homogeneous reactions are in instantaneous equilibrium, we have the following mass action equation [24, 25]:

$$C_i = (\gamma_i)^{-1} K_i \prod_{j=1}^{N_c} \left(\gamma_j C_j\right)^{\nu_{ji}}, \qquad (25)$$

where ν_{ji} are the stoichiometric coefficients, K_i is the equilibrium constant of the ith homogeneous reaction, γ_i is the activity coefficient of the ith secondary species, and C_j and C_i are solute concentrations for primary and secondary species, respectively. They are related to by

$$\Psi_j = C_j + \sum_{i=1}^{N_R} \nu_{ji} C_i , \tag{26}$$

where N_R is the number of independent homogeneous reactions, or, equivalently, secondary species.

More details on the heterogeneous reactions between aqueous species and minerals at the pore-mineral interface described by Eq. (10), and on the update of solid phase can be found in [22, 26]

3.4 Lattice Poisson Method

To solve the Poisson equation with strong nonlinearity, Eq. (9), we adopt the lattice Poisson method (LPM) developed previously [27, 28], which tracks the electrical potential distribution transporting on the discrete lattices. By expanding Eq. (9) into the time-dependent form

$$\frac{\partial \psi}{\partial t} = \nabla^2 \psi + g_{rhs}(\mathbf{r}, \psi, t)$$

with $g_{rhs} = \frac{1}{\varepsilon \varepsilon_0} \sum_i z_i e n_{i,\infty} \exp\left(-\frac{z_i e}{k_b T} \psi \right)$ representing the *negative* right hand side (RHS) term of the original Eq. (9), we get the discrete evolution equation for the electrical potential distribution

$$g_\alpha(\mathbf{r} + \Delta\mathbf{r}, t + \delta_{t,g}) - g_\alpha(\mathbf{r}, t) = -\frac{1}{\tau_g}\left[g_\alpha(\mathbf{r}, t) - g_\alpha^{eq}(\mathbf{r}, t) \right] + (1 - \frac{0.5}{\tau_g}) \delta_{t,g} \omega_\alpha g_{rhs} , \tag{27}$$

where g_α^{eq} is the equilibrium distribution of the electric potential evolution variable. The time step for the electrical potential evolution is

$$\delta_{t,g} = \frac{\delta_x}{c'}, \tag{28}$$

where c' is a *pseudo* sound speed in the potential field. After evolving on the discrete lattices, the mesoscopic electrical potential can be calculated using

$$\psi = \sum_\alpha (g_\alpha + 0.5\delta_{t,g} g_{rhs} \omega_\alpha). \tag{29}$$

Although the electrical potential evolution equations are in an unsteady form, only the steady state result is realistic, because the electromagnetic susceptibility has not been considered. Although the lattice evolution method for nonlinear Poisson equation is not as efficient as the multi-grid solutions due to its long wavelength limit, it has the advantages of suitability for geometrical complexity and parallel computing.

4. Simulation Examples

4.1 Injection of CO_2 into a limestone rock

We first present some modeling results on the injection of a fluid saturated with 170 bars CO_2(g) into a limestone rock at the pore scale. The pore structure was derived from a digitized image of a limestone rock thin section with 640×480 pixels (figure 1). We reduced the original resolution to save computational time (figure 2). The chemical system of Na^+-Ca^{2+}-Mg^{2+}-H^+-SO_4^{2-}-Cl^--CO_2 with the reaction of calcite to form dolomite and gypsum is considered. Secondary species included in the simulation are: OH^-, HSO_4^-, H_2SO_4(aq), CO_3^{2-}, HCO_3^-, $CaCO_3$(aq), $CaHCO_3^+$, $CaOH^+$, $CaSO_4$(aq), $MgCO_3$(aq), $MgHCO_3^+$, $MgSO_4$(aq), $MgOH^+$, NaCl(aq), $NaHCO_3$(aq), NaOH(aq). Initial fluid composition is pH 7.75 and 2.69 m NaCl brine,

233 equilibrium with minerals calcite, dolomite and gypsum at 25 °C. Initial rock composition is
234 calcite. Secondary minerals include dolomite and gypsum. For boundary conditions, a constant
235 pressure gradient is imposed across the domain for flow. When flow reaches steady state, a fluid
236 with a pH of 3.87 and in equilibrium with 179 bars $CO_2(g)$ and minerals dolomite and gypsum is
237 introduced at the inlet. Zero gradient boundary conditions are imposed at the outlet. Two
238 different cases are considered with different mineral reaction rates to show their effects on
239 solution concentration, mineral deposition and change in geometry.

240 Resulting geometries at time=15625 seconds for two different mineral reaction rate
241 constants are plotted in figure 3. Damkohler is 7.375 for calcite and gypsum and 0.7375 for
242 dolomite for the faster mineral reactions and 7.375×10^{-2} for calcite and gypsum and 7.375×10^{-3}
243 for dolomite for slower reactions. Concentration distribution of total Ca^{2+}, Mg^{2+}, and SO_4^{2-}, pH,
244 and reaction rates for calcite, dolomite, and gypsum for the slower reactions are plotted in figure
245 4. As can been seen from the figures, as the reaction rate constants decrease, the deposition of
246 dolomite becomes more uniform surrounding the dissolving calcite grains. Only a small amount
247 of gypsum forms on top of dolomite. At some point in the simulation, the major pores for flow
248 become blocked halting further fluid flow through the medium. The pH is uniform over the
249 entire pore space. All reaction rates have finite values at the mineral surface in the whole
250 domain, outlining the solid geometry. The reaction rate is negative for calcite and positive for
251 dolomite and gypsum, confirming that calcite is dissolving while dolomite and gypsum are
252 precipitating.

253 ***4.2 Two-phase behavior and flooding phenomena in polymer electrolyte fuel cells***

254 In this Section, we present some results for two-phase flow through the porous CL and
255 the fibrous GDL in a PEFC. Details can be found in [29]. Figure 5 displays the steady state

256 invading liquid water fronts corresponding to increasing capillary pressures from the primary
257 drainage simulation in the reconstructed CL microstructure characterized by slightly
258 hydrophobic wetting characteristics with a static contact angle of 100°. At lower capillary
259 pressures, the liquid water saturation front exhibits finger like pattern, similar to the
260 displacement pattern observed typically in the capillary fingering regime. The displacing liquid
261 water phase penetrates into the body of the resident wetting phase (i.e. air) in the shape of fingers
262 owing to the surface tension driven capillary force. However, at high saturation levels, the
263 invading non-wetting phase tends to exhibit a somewhat flat advancing front. This observation,
264 as highlighted in figure 5(b), indicates that with increasing capillary pressure, even at very low
265 capillary number (Ca), several penetrating saturation fronts tend to merge and form a stable
266 front. The invasion pattern transitions from the capillary fingering regime to the stable
267 displacement regime and potentially lies in the transition zone in between. In an operating fuel
268 cell, the resulting liquid water displacement pattern pertaining to the underlying pore-
269 morphology and wetting characteristics would play a vital role in the transport of the liquid water
270 and hence the overall flooding behavior.

271 Figure 6 shows the liquid water distribution as well as the invasion pattern from the
272 primary drainage simulation with increasing capillary pressure in the initially air-saturated
273 reconstructed carbon paper GDL characterized by hydrophobic wetting characteristics with a
274 static contact angle of 140°. The reconstructed GDL structure used in the two-phase simulation
275 consists of 100×100×100 lattice points in order to manage the computational overhead to a
276 reasonable level. Physically, this scenario corresponds to the transport of liquid water generated
277 from the electrochemical reaction in a hydrophobic CL into the otherwise air-occupied GDL in
278 an operating fuel cell. At the initially very low capillary pressure, the invading front overcomes

279 the barrier pressure only at some preferential locations depending upon the pore size along with
280 the emergence of droplets owing to strong hydrophobicity. As the capillary pressure increases,
281 several liquid water fronts start to penetrate into the air occupied domain. Further increase in
282 capillary pressure exhibits growth of droplets at two invasion fronts, followed by the coalescence
283 of the drops and collapsing into a single front. This newly formed front then invades into the less
284 tortuous in-plane direction. Additionally, emergence of tiny droplets and subsequent growth can
285 be observed in the constricted pores in the vicinity of the inlet region primarily due to strong wall
286 adhesion forces from interactions with highly hydrophobic fibers with the increasing capillary
287 pressure. One of the several invading fronts finally reaches the air reservoir, physically the
288 GDL/channel interface, at a preferential location corresponding to the capillary pressure and is
289 also referred to as the bubble point. It is important to note that the mesoscopic LB simulations
290 provide fundamental insight into the pore-scale liquid water transport through different GDL
291 structures and would likely enable novel GDL design with better water removal and flooding
292 mitigation.

293 ***4.3 Electroosmosis in homogeneously charged micro- and nano-scale porous media***

294 In this section, we briefly present some simulation results on electroosmotic flows
295 (EOFs) in charged micro porous media using the lattice Poisson-Boltzmann method (LPBM),
296 with geometry effects, solution and surface charge effects considered. More details can be found
297 in [28]. We focus on a cubic system of which each side is 1 micron long. A 60×60×60 uniform
298 grid is used. We change microstructure geometries of porous media by varying the porosity ε
299 from 0.1 to 0.9. The average characteristic length of particles varies from 20 to 150 nm. Figure 7
300 shows Schematics of the generated porous structures for porosity 0.3 and 0.6. The bulk ionic
301 concentration n_∞ varies from 10^{-6} to 10^{-3} M and the surface zeta potential from 0 to -100 mV.

302 The other properties and parameters used in this work are: the fluid density ρ=999.9 kg/m^3, the
303 dielectric constant $\varepsilon_r\varepsilon_0$=6.95×10^{-10} C^2/J m, the dynamic viscosity μ=0.889 mPa s, the
304 temperature T=273 K and the external electrical field strength E=1×10^4 V/m.
305 First, the geometry effects on the electroosmotic permeability in micro porous media are
306 investigated by changing volume fraction and particle size (or number density) of the solid
307 phase. We define the electroosmotic permeability, κ_e, as

308 $$\kappa_e = \frac{\bar{u}}{E}, \tag{30}$$

309 where $\bar{u}$ is the averaged velocity of EOF along the direction of the driving electrical field $\mathbf{E}$.
310 The coefficients of electroosmotic permeability (κ_e) for different porosities (ε) of porous media
311 are shown in figure 8. The bulk molar concentration c_∞=10^{-4} M, and ζ = -50 mV. The
312 electroosmotic permeability increases with the porosity monotonically. The increasing rate rises
313 with the porosity as well which is very low when the porosity is smaller than 0.5 and becomes
314 sharply high when the porosity is larger than 0.7. The predicted electroosmotic permeability is in
315 the order of 10^{-9} m^2/s V, which is consistent with the existing experimental measurements.
316 Figure 9 shows the predicted electroosmotic permeability versus the bulk ionic
317 concentration of the electrolyte solution. We used ε=0.38. The electroosmotic permeability κ_e
318 increase monotonically with the bulk ionic concentration c_∞ as c_∞ varies from 10^{-6} to 10^{-3} M.
319 This result can be explained by the undeveloped electrical potential distributions in narrow
320 channels, whose similar results can be found in Fig. 2 of Ref. [30] and Fig.1&2 of Ref. [31].
321 When c_∞ is lower than 10^{-4} M, the electroosmotic permeability is nearly proportional to the bulk
322 ionic concentration. When c_∞ is higher, the increasing rate becomes a little smaller.

Zeta potential on solid surfaces of porous media affects EOF permeability directly. Simple proportional relationships have been obtained between the electroosmotic permeability and the zeta potential for electrical transports in soils and in polymer composites recently based on the boundary-layer theory. Here we analyze such effects using our numerical methods.

Figure 10 shows the calculated electroosmotic permeability versus the zeta potential on solid surfaces of porous media. All surfaces are homogeneously charged with a same value of ζ. The other parameters used are: $c_\infty = 10^{-4}$ M, $c_d = 0.1$ and $\varepsilon = 0.38$. The zeta potential ζ changes from 0 to 100 mV. It shows that the proportionally linear relationship between electroosmotic permeability and zeta potential is accurate only when ζ is very small (<30 mV). The permeability increases much sharper when the zeta potential ζ is larger than 40 mV and then smoother when the zeta potential ζ is larger than 90 mV.

5. Conclusions

We have presented our recent work on mesoscopic modeling of multi-physicochemical processes in porous media, based on the LBM. For the problem of injecting CO_2 saturated brine into a limestone rock, it is shown that the LBM is able to provide detailed information on fluid velocity, solute concentration, mineral composition, and reaction rates, as well as the evolution of the porous media geometry, and therefore can shed some light on the fundamental physics occurring at the pore scale for reactive transport involved in geologic CO_2 sequestration. For two-phase behavior and flooding phenomena in PEFCs, the LBM is a powerful tool to study the influence of the pore structure and surface wettability on liquid water transport and interfacial dynamics in the PEFC catalyst layer and gas diffusion layer. Particularly, the two-phase regime transition phenomenon in the capillary dominated transport in the CL and the influence of the mixed wetting characteristics on the flooding dynamics in the GDL are demonstrated. For

electroosmotic flows in charged porous media, the strongly nonlinear governing equations of electroosmosis in three-dimensional porous media are solved using the LPBM. The effects of pore structure, bulk ionic concentration, and the surface charge on electroosmotic permeability are carefully investigated. It is concluded that the LBM is a powerful numerical tool to simulate multi-physicochemical processes in porous media at the pore-scale.

Acknowledgements

This article is based on research project supported by the National Science Foundation under Grant No. CHE-0431328 and the U.S. Department of Energy, Biological and Environmental Research (BER), and by LDRD projects 20070760PRD4 and 20080727PRD2 sponsored by Los Alamos National Laboratory.

References

1. Pacala, S. and R. Socolow, *Stabilization wedges: Solving the climate problem for the next 50 years with current technologies.* SCIENCE, 2004. **305**(5686): p. 968-972.
2. Bear, J., *Dynamics of Fluids in Porous Media.* 1972, New York: Elsevier. 536.
3. Wang, C.-Y., *Fundamental Models for Fuel Cell Engineering.* Chemical Reviews, 2004. **104**(10): p. 4727-4766.
4. Baschuk, J.J. and X. Li, *Modelling of polymer electrolyte membrane fuel cells with variable degrees of water flooding.* Journal of Power Sources, 2000. **86**(1-2): p. 181-196.
5. You, L. and H. Liu, *A two-phase flow and transport model for the cathode of PEM fuel cells.* International Journal of Heat and Mass Transfer, 2002. **45**(11): p. 2277-2287.
6. He, W., J.S. Yi, and T.V. Nguyen, *Two-phase flow model of the cathode of PEM fuel cells using interdigitated flow fields.* AIChE Journal, 2000. **46**(10): p. 2053-2064.
7. Nam, J.H. and M. Kaviany, *Effective diffusivity and water-saturation distribution in single- and two-layer PEMFC diffusion medium.* International Journal of Heat and Mass Transfer, 2003. **46**(24): p. 4595-4611.
8. Dutta, S., S. Shimpalee, and J.W. Van Zee, *Numerical prediction of mass-exchange between cathode and anode channels in a PEM fuel cell.* International Journal of Heat and Mass Transfer, 2001. **44**(11): p. 2029-2042.
9. Noponen, M., et al., *A Two-Phase Non-Isothermal PEFC Model: Theory and Validation.* Fuel Cells, 2004. **4**(4): p. 365-377.
10. Wang, Z., et al., *Binocular fusion in Panum's limiting case of stereopsis obeys the uniqueness constraint.* Science in China Series C: Life Sciences, 2001. **44**(1): p. 40-48.
11. Chen, S. and G.D. Doolen, *Lattice Boltzmann method for fluid flows.* Annual Review of Fluid Mechanics, 1998. **30**: p. 329-364.

12. Landau, L.D. and E.M. Lifshitz, *Fluid Mechanics*. 1959, New York: Elsevier. 536.
13. Lichtner, P.C., *Principles and practice of reactive transport modeling.* Mat. Res. Soc. Symp. Proc., 1995. **353**: p. 117-130.
14. Levich, V.G., *Physico-Chemical Hydrodynamics*. 1962, New York: Prentice-Hall.
15. Honig, B. and N. A., *Classical electrostatics in biology and chemistry.* Science, 1995. **268**(5214): p. 1144-1149.
16. Lichtner, P.C. and Q. Kang, *Upscaling Pore-Scale Reactive Transport Equations using a Multi-Scale Continuum Formulation.* Water Resources Research, 2007. **43**(W12S15): p. doi:10.1029/2006WR005664.
17. Guo, Z.L., B.C. Shi, and N.C. Wang, *Lattice BGK model for incompressible Navier-Stokes equation.* Journal of Computational Physics, 2000. **165**(1): p. 288-306.
18. Shan, X. and H. Chen, *Lattice Boltzmann model for simulating flows with multiple phases and components.* PHYSICAL REVIEW E, 1993. **47**(3): p. 1815.
19. Kang, Q., D. Zhang, and S. Chen, *Displacement of a two-dimensional immiscible droplet in a channel.* Physics of Fluids, 2002. **14**: p. 3203.
20. Kang, Q., D. Zhang, and S. Chen, *Displacement of a three-dimensional immiscible droplet in a duct.* Journal of Fluid Mechanics, 2005. **545**: p. 41.
21. Shan, X. and G. Doolen, *Diffusion in a multicomponent lattice Boltzmann equation model.* PHYSICAL REVIEW E, 1996. **54**(4): p. 3614.
22. Kang, Q.J., P.C. Lichtner, and D.X. Zhang, *Lattice Boltzmann pore-scale model for multicomponent reactive transport in porous media.* JOURNAL OF GEOPHYSICAL RESEARCH-SOLID EARTH, 2006. **111**(B5).
23. Dawson, S.P., S. Chen, and G.D. Doolen, *Lattice Boltzmann computations for reaction-diffusion equations.* The Journal of Chemical Physics, 1993. **98**(2): p. 1514-1523.
24. Lichtner, P.C., C.I. Steefel, and E.H. Oelkers, eds. *Reactive transport in porous media.* Reviews in mineralogy, ed. P.H. Ribbe. Vol. 34. 1996, Mineralogical Society of America Washington, D. C.
25. Lichtner, P.C., *Continuum model for simultaneous chemical reactions and mass transport in hydrothermal systems.* GEOCHIMICA ET COSMOCHIMICA ACTA, 1985. **49**(3): p. 779-800.
26. Kang, Q., P.C. Lichtner, and D. Zhang, *An improved lattice Boltzmann model for multicomponent reactive transport in porous media at the pore scale.* WATER RESOURCES RESEARCH, 2007. **43**(12).
27. Wang, J.K., M. Wang, and Z.X. Li, *Lattice Poisson-Boltzmann simulations of electro-osmotic flows in microchannels.* Journal of Colloid and Interface Science, 2006. **296**(2): p. 729-736.
28. Wang, M. and S. Chen, *Electroosmosis in homogeneously charged micro- and nanoscale random porous media.* Journal of Colloid and Interface Science, 2007. **314**(1): p. 264-273.
29. Mukherjee, P.P., C.-Y. Wang, and Q. Kang, *Mesoscopic modeling of two-phase behavior and flooding phenomena in polymer electrolyte fuel cells.* Electrochimica Acta, 2009. **54**(27): p. 6861-6875.
30. Wang, M., et al., *Lattice Poisson-Boltzmann simulations of electroosmotic flows in charged anisotropic porous media.* Communications in Computational Physics, 2007. **2**: p. 1055-1070.

31. Wang, M.R., J.K. Wang, and S.Y. Chen, *Roughness and cavitations effects on electro-osmotic flows in rough microchannels using the lattice Poisson-Boltzmann methods.* Journal of Computational Physics, 2007. **226**(1): p. 836-851.

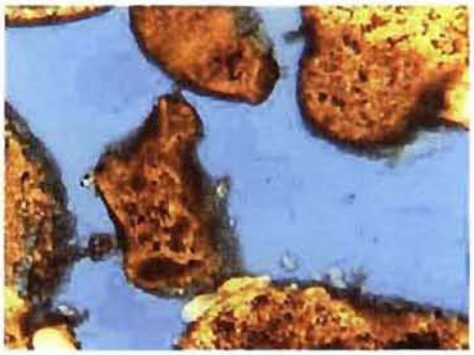

Figure 1 Photographic image of a limestone rock thin section (640x480 pixels).

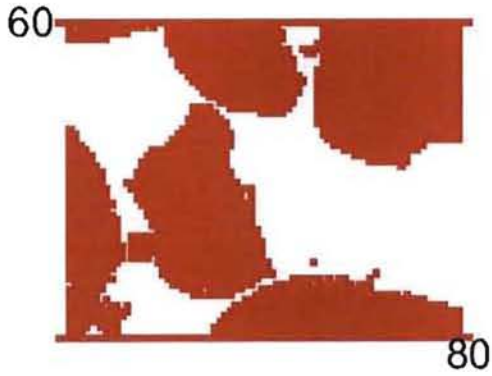

Figure 2 Digitized image with reduced resolution.

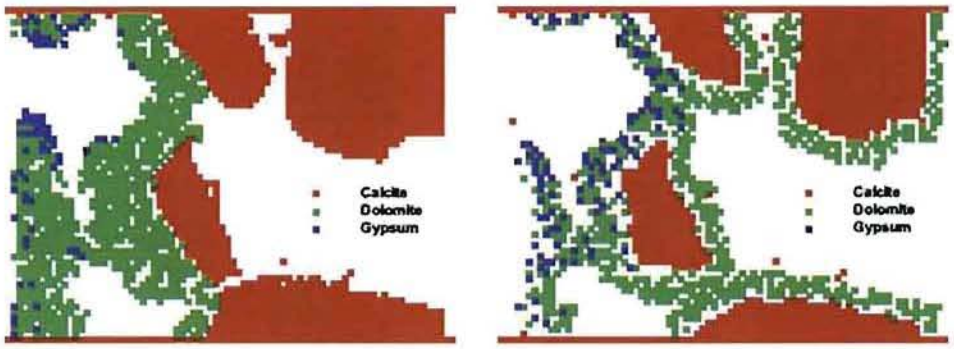

Figure 3 Resulting geometries at time=15625 seconds for two different mineral reaction rate constants: a) large reaction rate constants; b) small reaction rate constants.

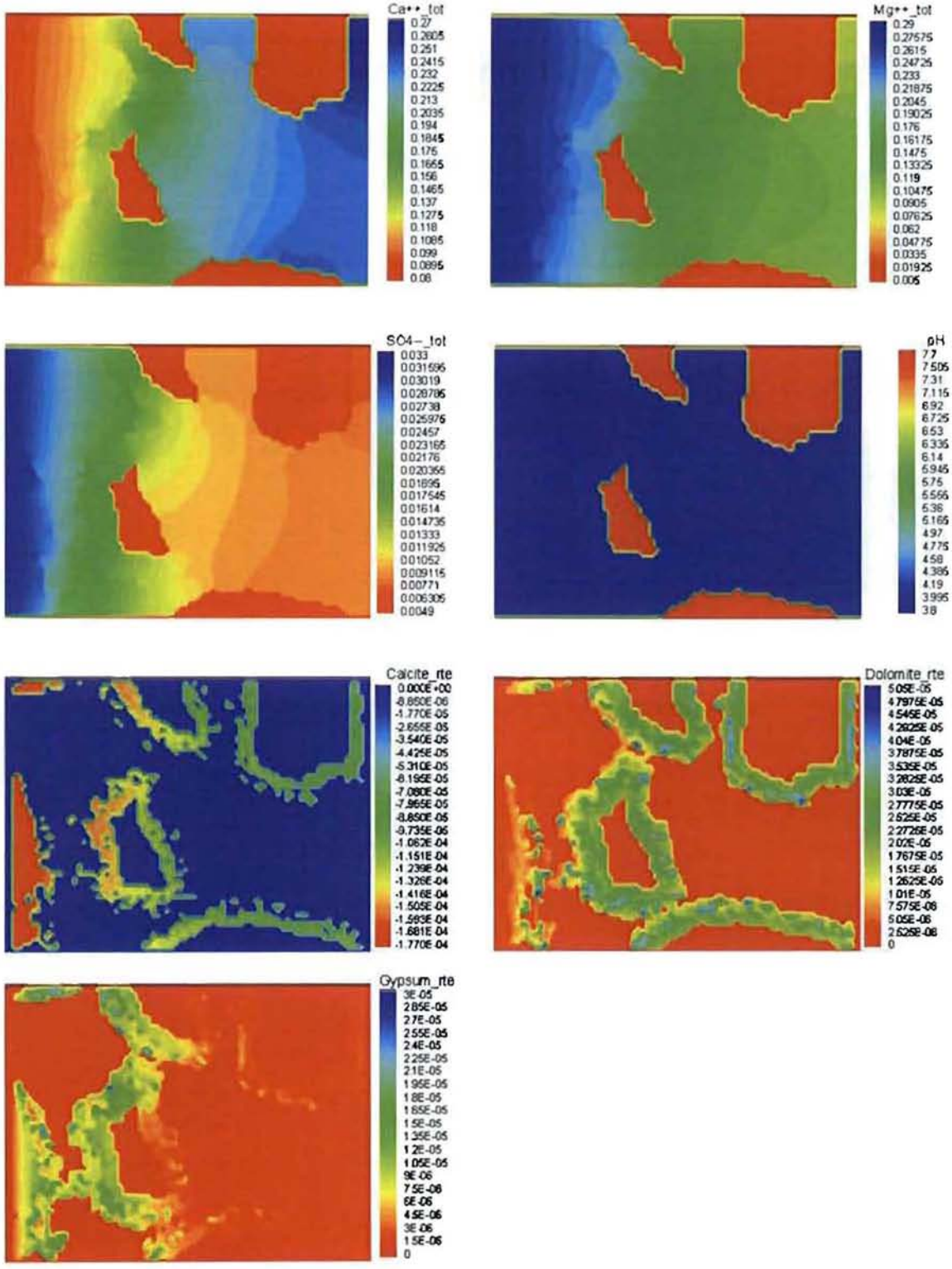

Figure 4 Distribution of solute concentrations, pH value, and reaction rates at time=15625 seconds for small reaction rate constants.

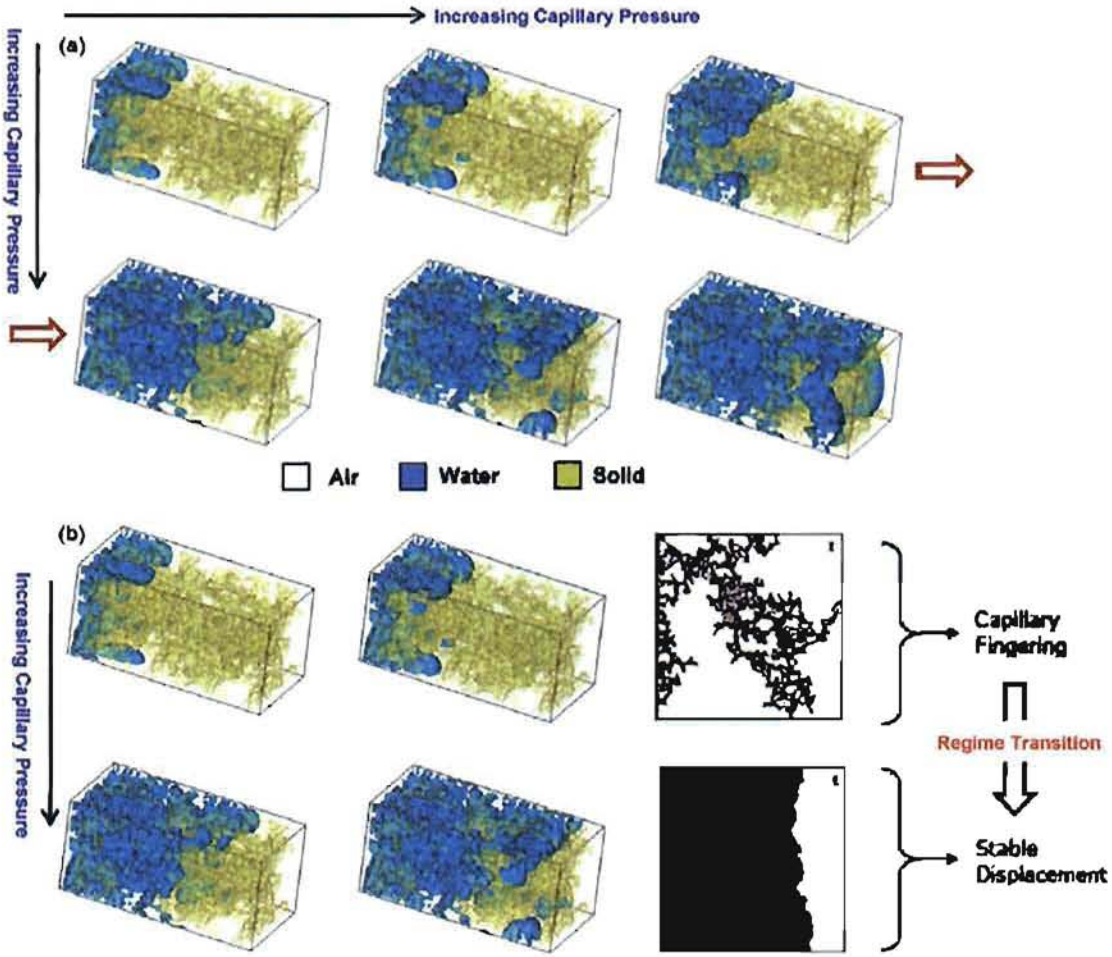

Figure 5 Advancing liquid water front with increasing capillary pressure through the initially air-saturated reconstructed CL microstructure from the primary drainage simulation.

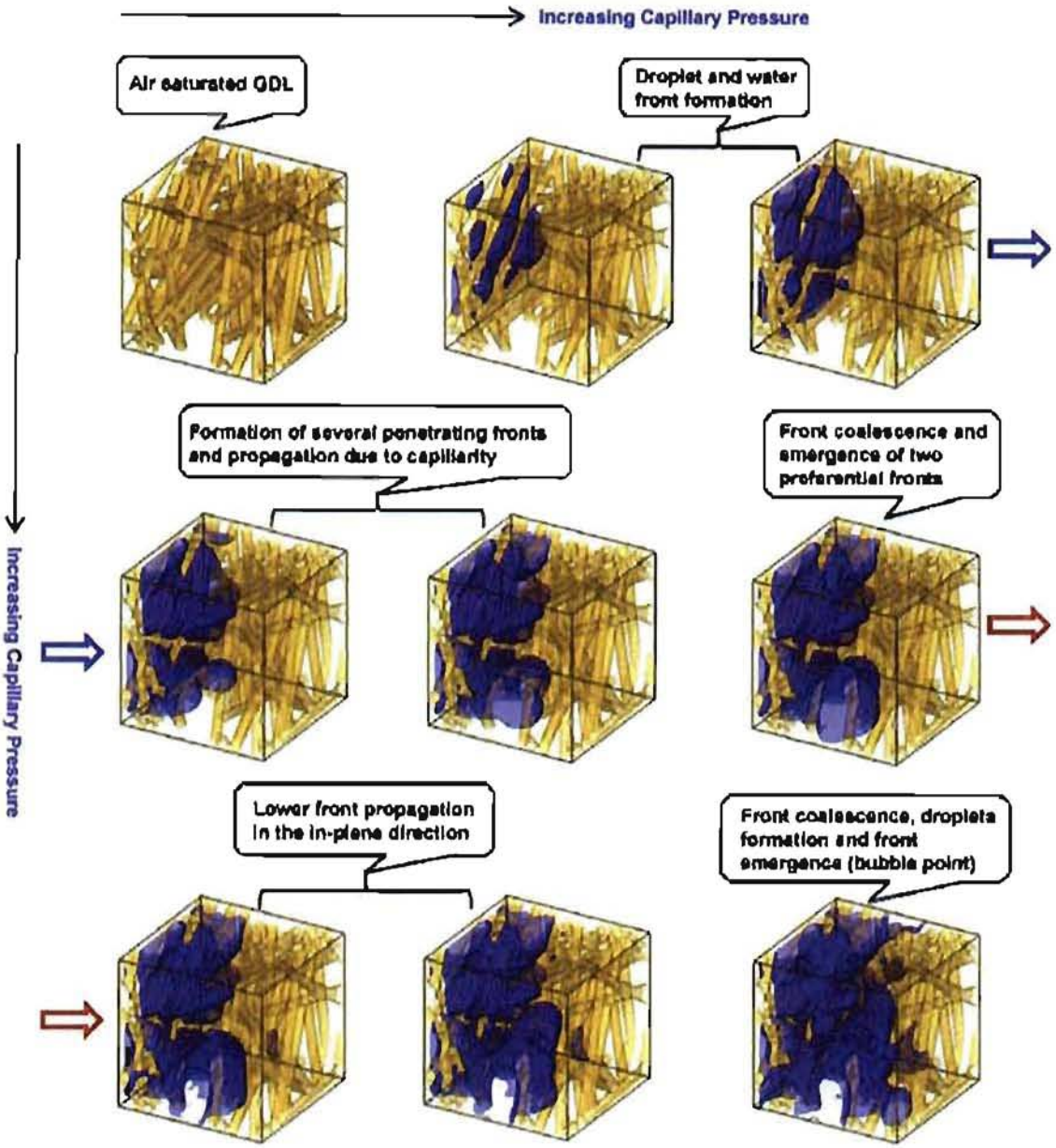

Figure 6 Advancing liquid water front with increasing capillary pressure through the initially air-saturated reconstructed GDL microstructure from the primary drainage simulation.

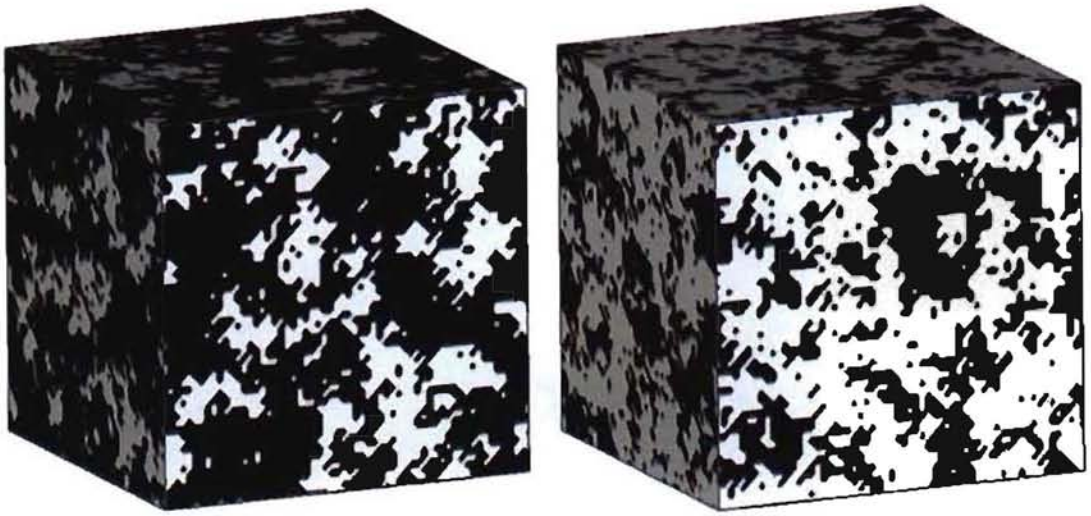

Figure 7 Schematics of the generated porous structures on 60×60×60 grid systems. The white is solid particles and the dark is fluid: a) porosity=0.6; b) porosity=0.3.

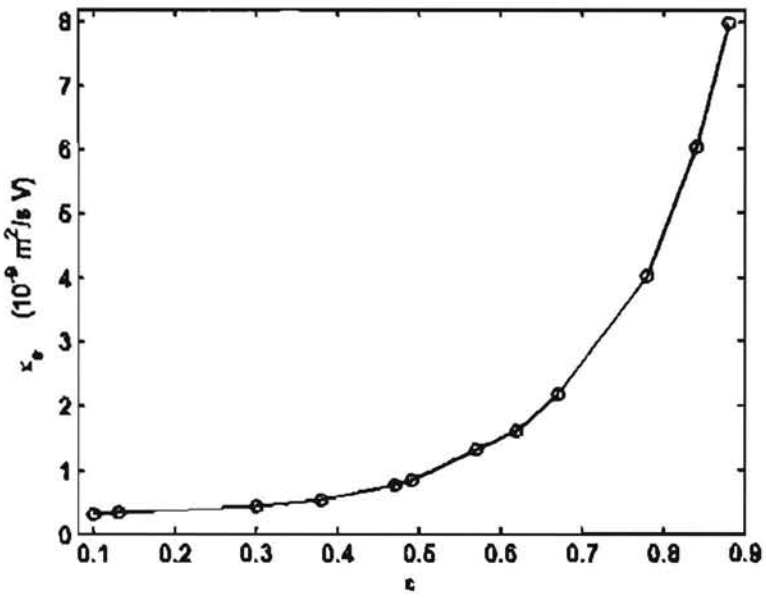

Figure 8 Predicted electroosmotic permeabilities for various porosities of porous media at $c_\infty = 10^{-4}$ M, $\zeta = -50$ mV, $E = 1 \times 10^4$ V/m.

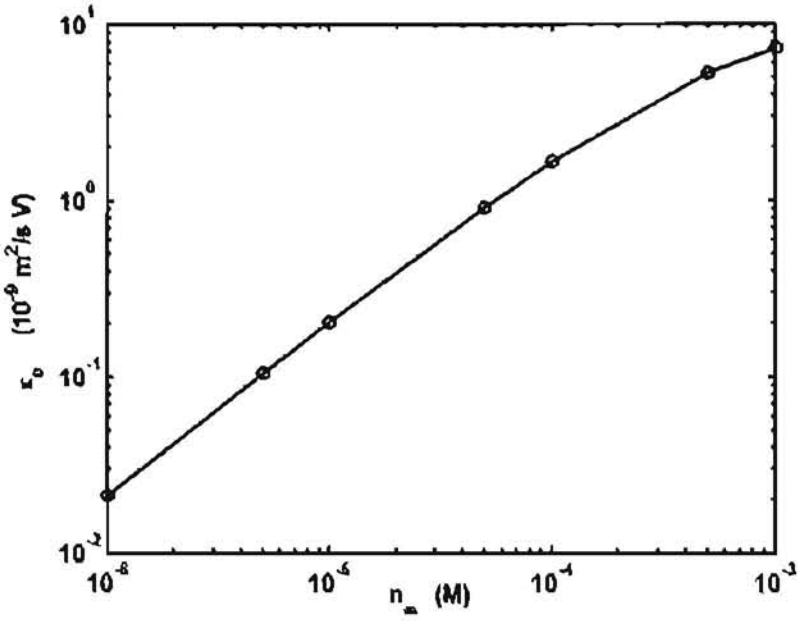

Figure 9 The electroosmotic permeability changing with the bulk ionic concentration for ε=0.38, ζ = -50 mV, and E =1×10^4 V/m.

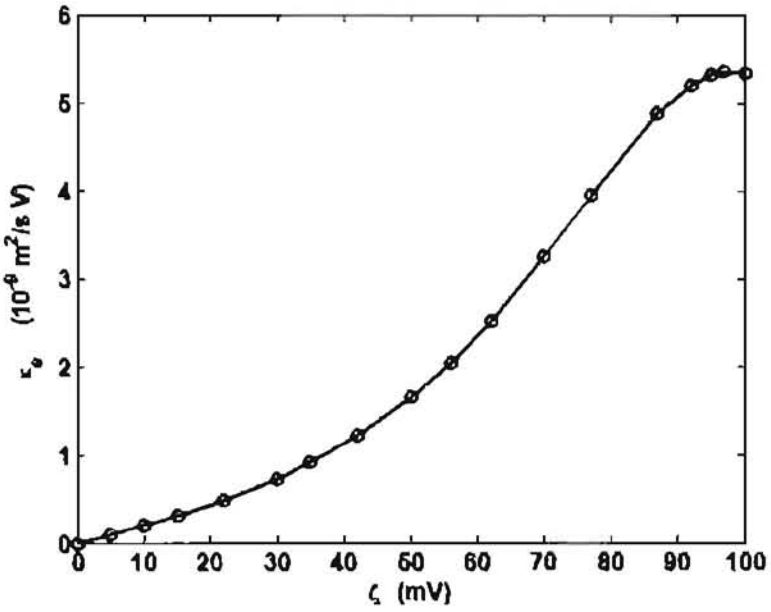

Figure 10 The electroosmotic permeability versus the zeta potential for ε=0.38, c_∞=10^{-4} M, and E=1×10^4 V/m.